Eur. Phys. J. D (2015) 69: 251
DOI: 10.1140/epjd/e2015-60443-6

THE EUROPEAN PHYSICAL JOURNAL D

Regular Article

Field emission driven direct current argon discharges and electrical breakdown mechanism across micron scale gaps*

Štefan Matejčik[1], Branislav Radjenović[2], Matej Klas[1], and Marija Radmilović-Radjenović[2,a]

[1] Department of Experimental Physics, Comenius University, Mlynska dolina F2, 84248 Bratislava, Slovakia
[2] Institute of Physics, University of Belgrade, Pregrevica 118, 11080 Zemun, Serbia

Received 30 July 2015 / Received in final form 8 September 2015
Published online 12 November 2015 –

Abstract. In this paper results of the experimental and theoretical studies of the field emission driven direct current argon microdischarges for the gaps between 1 μm and 100 μm are presented and discussed. The breakdown voltage curves and Volt-Ampere characteristics proved to be a fertile basis providing better understanding of the breakdown phenomena in microgaps. Based on the measured breakdown voltage curves, the effective yields have been estimated confirming that the secondary electron emission due to high electric field generated in microgaps depends primarily on the electric field leading directly to the violation of the Paschen's law. Experimental data are supported by the theoretical predictions that suggest departure from the scaling law and a flattening of the Paschen curves at higher pressures confirming that Townsend phenomenology breaks down when field emission becomes the key mechanism leading to the breakdown. Field emission of electrons from the cathode, the space charge effects in the breakdown and distinction between the Fowler-Nordheim field emission and the space charge limited current density are also analyzed. Images and Volt-Ampere characteristics recorded at the electrode gap size of 20 μm indicate the existence of a discharge region similar to arc at the pressure of around 200 Torr has been observed.

1 Introduction

Studies of the microdischarges based on the narrow electrode gaps and high pressure properties are relevant for a wide range of promising applications, such as light sources, sensors, material processing and synthesis, chemical analysis, environmental applications and medical treatments [1–10]. The microdischarges are similar to the conventional discharges at larger scales in many ways, but have some important differences. As the distance between the electrodes is decreased, the pressure at which lower currents and stable discharges exist is increased, up to and exceeding the atmospheric pressure. Since the microplasmas are usually in non-thermal equilibrium so the electron temperatures can be very high, while the other species remain at low temperatures, they are well-suited to treat heat sensitive surfaces [11–13]. However, due to the small dimensions, investigations with optical diagnostics in microplasma discharges are very challenging [14,15].

Similarity and scaling laws are effective tools for estimation of the discharge conditions from those in large scale low-pressure discharges to the operation of a down-scaled discharge [16–18]. Due to the simple and well-defined geometry, the parallel plate direct-current (DC) micro discharge represents an ideal configuration for benchmarking models and for checking similarities with the larger scale low-pressure discharges. Although numerous studies and publications for the low-pressure standard size parallel plate discharges exist, for the parallel plate DC micro discharges, only a few theoretical and experimental studies exist. The scaling of the voltage-current characteristic [19,20] and Paschen's law [21] were verified for the micro discharges.

The main approach in generating a micro-discharge in atmospheric pressure is based on scaling law [22,23]. Scaling should be related to the *pd* product (*the pressure* × *the electrode separation*) meaning that in order to ignite a plasma at atmospheric pressure the inter electrode gap dimensions have to be scaled down to the micrometer range. According to the Townsend's theory, the Paschen curve represents the voltage needed to achieve a balance between the number of electrons lost by diffusion and drift in the inter-electrode gap and the number of secondary electrons generated at the cathode [24]. Over a wide range of pressures and electrode separations, the probability of ionization per electron-neutral collision in the gas and the probability of the secondary electron production at the

* Contribution to the Topical Issue "Recent Breakthroughs in Microplasma Science and Technology", edited by Kurt Becker, Jose Lopez, David Staack, Klaus-Dieter Weltmann and Wei Dong Zhu.

[a] e-mail: marija@ipb.ac.rs

cathode by ion impact are proportional to the reduced electric field and lead to the well-established *pd* similarity law. The departures from the similarity law, however, are observed in the microgaps indicating that Paschen curves do not offer sufficient information in the case of very small separations [25,26]. Therefore it is necessary to determine volt-ampere (V-A) characteristics of the DC micro-discharges for proper understanding the process of breakdown [27,28].

In this paper the breakdown voltage phenomena in DC argon microdischarges have been investigated experimentally and theoretically. The breakdown voltage curves were recorded at the gap sizes from 1 μm and 100 μm. Based on the recorded breakdown voltage curves, the dependence of the effective yields on the reduced electric field and on the electric field have been estimated. The expression for the breakdown voltage in microgaps has been applied in order to calculate the gap size and pressure dependences of the breakdown voltage for gaps less than 1 μm. Results for the gaps of a few microns have been analyzed via Fowler-Nordheim theory for the field emission. The effect of the different parameters on the current density has been studied and compared with the space charge limited current. Volt-Ampere characteristics recorded at the electrode gap size of 20 μm suggest the existence of micro-arc plasma discharges operating at the pressures of around 200 Torr.

2 Theoretical background

2.1 Field emission

In general, field emission (FE) represents the extraction of electrons from a solid by tunneling through the surface-potential barrier under the influence of a strong electric field, such as field generated in the microgaps [29,30]. FE is recognized as the most important factor in breakdown initiation in small gaps and can be described as the ejection of electrons from the surface at high-field strengths [31–33]. When the electric field becomes sufficiently large, an ion that approaches the cathode could narrow the potential barrier seen by the electrons in the metal resulting in an ion-enhanced electron field emission. An explicit expression for the effective secondary electron emission coefficient γ' that includes this ion-enhanced field emission is [34]:

$$\gamma' = Ke^{-D/E}, \tag{1}$$

where K and D are material and gas dependent constants and E the electric field near the cathode. According to equation (1), when the electric field in the cathode region exceeds the threshold value given by D, the secondary electron emission coefficient increases rapidly and consequently the breakdown voltage decreases. Constant K can be determined from the ratio of the field emission current density to the positive ion current density onto the cathode. On the other hand, constant D can be calculated by using the expression [35]:

$$D = 6.85 \times 10^7 \phi^{3/2} \beta, \tag{2}$$

where β is a field enhancement factor and ϕ is the work function of the metal i.e. minimum energy required to remove an electron from the surface of the material expressed in eV.

The equation that governs the mechanism of the DC breakdown in micrometer gaps [36] is:

$$V_{DC} = \frac{d(D + Bp)}{\ln[ApdK]}, \tag{3}$$

where d and p represent the interelectrode distance and the gas pressure, respectively, while A and B are gas specific constants [37,38].

The resulting current of electrons is not uniformly distributed over the cathode region and there are also local regions that contribute to the current. In order to characterize such regions, it is convenient to introduce the enhancement factor β defined as the ratio of the local emitter field over the applied field. This factor is often introduced in the F-N equation to represent the geometrical effects at the surface of the cathode [39–41]. In principle, factor β has a direct physical meaning only for metallic protrusions. If the shape of the protrusion is reasonably simple, value of the enhancement factor can be calculated quite accurately.

The Fowler-Nordheim (F-N) law gives the current density extracted from a surface under strong fields, by treating the emission of electrons from a metal-vacuum interface in the presence of an electric field normal to the surface as a quantum mechanical tunneling process. The F-N equation provides a theoretical relation between the current density of field emission electrons j_{FE} and the electric field at the surface of the emitter:

$$j_{FE} = \frac{6.2 \times 10^{-6} (\beta E)^2}{\phi \tau^2} \exp\left(-\frac{6.85 \times 10^7 \phi^{3/2} \Theta}{\beta E}\right), \tag{4}$$

where only the function ϕ is controlling quantity that depends on the emission surface. The impact due to changes of a tunneling barrier shape on the exponential term in the F-N equation are included through corrections:

$$\Theta(y) = 0.95 - \upsilon^2, \ \tau^2(\upsilon) \approx 1.1, \ \ \upsilon \approx 3.79 \times 10^{-4} \sqrt{\beta E}/\phi. \tag{5}$$

Field emission results are more conventionally shown on F-N plot [42]:

$$\ln\left(\frac{I_{FE}}{V^2}\right) = \Upsilon - \frac{1}{V}\xi, \tag{6}$$

$$\Upsilon = A_e \frac{1.54 \times 10^6 \beta^2}{\phi \times d^2} \exp\left(\frac{10.41}{\phi^{1/2}}\right), \tag{7}$$

$$\xi = \frac{6.53 \times 10^3 \times \phi^{3/2}}{\beta/d} \approx \frac{\text{constant}}{\beta}. \tag{8}$$

In the scenario of electron field emission, the F-N plot should fit a straight line. The numerical value of β can be determined by using the expression for the slope:

$$\frac{d(\log_{10} I_{FE}/E^{2.5})}{d(1/E)} = -\frac{-2.84 \times 10^9 \phi^{1.5}}{\beta}. \tag{9}$$

Since enhancement factor usually varies locally on the cathode surface, instead of the constant β it is customary to calculate the effective enhancement factor β_{eff} by solving the equation [43]:

$$\int_0^l \frac{A(\beta(y)E_0)^2}{\phi\tau^2(y')} \exp\left(\frac{-Bv(y')\phi^{3/2}}{\beta(y)E_0}\right) dy = \int_0^l \frac{A(\beta_{\text{eff}}E_0)^2}{\phi\tau^2(y')} \exp\left(\frac{-Bv(y')\phi^{3/2}}{\beta_{\text{eff}}E_0}\right) dy, \quad (10)$$

where l is the cathode length, $\beta(y)$ is the local enhancement factor distribution and E_0 is the initial surface electric field.

2.2 Space charge

The value of the field emission current is closely related to the space charge of electrons leaving the cathode that effectively reduces field in front of the cathode, inhibiting the electron flow from the cathode and limiting the current density. The space charge caused by the cathode may affect the current density-voltage characteristics predicted by the F-N theory. Child's law predicts the maximum transmitted current density by considering the space charge effect. When the electric field becomes high enough, the emitted current density j_{CL} will be limited by Child's law [40,43]:

$$j_{CL} = \frac{4\varepsilon_0}{9}\sqrt{\frac{2e}{m}}\frac{V^{3/2}}{d^2}. \quad (11)$$

At higher pressures such as atmospheric pressure, an avalanche increase in the discharge leads to rise of a space charge, which alters the character of the breakdown process. The space charge field can be calculated as:

$$E_+ \approx \frac{e_+ d}{2\varepsilon_0} \approx \frac{j_+ d}{2\varepsilon_0 v_+}, \quad (12)$$

where n_+ and j_+ represent the ion and ion current densities, respectively and v_+ is the ion drift velocity.

3 Experimental arrangement

Measurements were carried out by the experimental set-up similar to the one described in our previous publications (see, for example, [28,32,40,44]) and shown in Figure 1. The discharge system consists of two planar molybdenum electrodes 2 mm in diameter and separated between 1 μm and 100 μm. Measurements were carried out using melted glass covered molybdenum electrodes as shown in Figure 2a. Additionally in Figure 2b we present surface SEM picture of the electrode surface and glass electrode interface. The vacuum chamber itself consists of three parts: positioner for centering the electrode position in three directions and tilting the upper electrode which is located in the upper part. In the middle part there is a glass crux with four fused silica windows. In the bottom part there is also positioning system for tilting electrode as well as an improved system for very ultra fine tilting. The electrode system is fixed in the cradle with micrometric screw. One of the electrodes was fixed and the other was movable continuously with micrometer scale linear feed-through. Electrodes were highly polished and covered by dielectric glass cap in order to prevent discharge to ignite at longer paths.

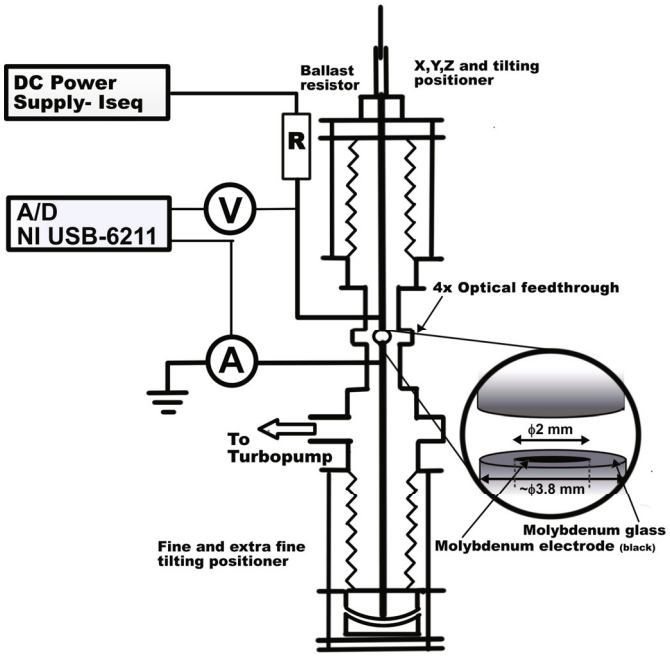

Fig. 1. General layout of the experimental set-up used for measurements of the direct current breakdown voltage in argon.

At the beginning of measurements, interface between molybdenum electrodes and the glass is smooth without any significant inhomogeneity as can be seen from Figure 2 so we assumed the distortion of the electric field is very low. During this stage, the breakdown voltages are more or less stable. However, after some time the breakdown voltages are unstable due to sputtering of molybdenum glass particles forming a dielectric layer on the electrode surfaces. This effect mostly increases breakdown voltages at higher pd. On the other side at low pd, the situation is opposite and we observed lower breakdown voltages. The reason is enlarged and deeper gap between electrode and glass due to evaporation and thus discharge can ignite on longer path.

The breakdown voltage curves were recorded based on the time dependence of the potential difference across the discharge tube by using a digital oscilloscope. After a very slowly increasing potential was applied to one of the electrodes, the potential across the discharge tube was increased until the breakdown occurs. The DC breakdown voltage was determined from the minimum potential across the discharge gap required for ignition. The fact that the breakdown voltage depends on the cathode

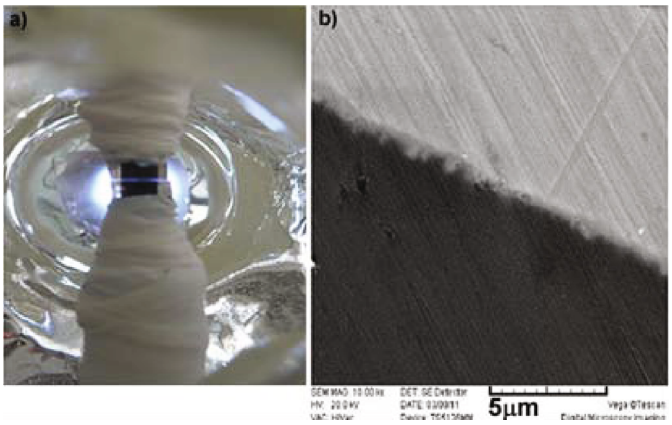

Fig. 2. (a) Molybdenum electrodes covered by melted glass. (b) SEM picture of the interface glass (light gray)-molybdenium (dark gray).

material has to be taken into account in breakdown measurements. Even more, the state of the cathode surface such as roughness or possible oxide layers and other impurities deposited on its surface either by exposing the cathode to the laboratory environment or during the discharge operation also have strong influence on the breakdown voltage curves. For recording voltage-current characteristics, we have used AD card (National Instruments NI USB-6211) with sampling frequency 10 kHz and averaging from 10 to 200 samples. The discharge sustained current was limited to 2 mA by power supply to prevent electrode surface destruction. The images were recorded by camera connected to a microscope.

4 Results and discussion

Figure 3a shows the breakdown voltage curve as a function of pd product for different electrode gaps ranging from 1 μm up to 100 μm. There is a good agreement between present experimental results for 100 μm (black symbols) and the data for the centimeter gaps taken from reference [45] (dash dot curve) and [46] (dot curve), since field emission plays no role for such gap sizes. On the other hand, for the gaps less than 5 μm the breakdown voltages are systematically lower than those predicted by the standard Paschen law due to the field emission enhanced secondary electron production. Based on the measured breakdown voltage curves, the values of the effective yield versus the reduced electric field E/p (electric field to the gas pressure ratio) were determined [47]. Our values of the effective yields are in a good agreement with the data taken from reference [48] (open down triangles). As can be observed from Figure 3b, the lowest values of the yield were obtained for the 100 μm gaps (crosses). With decreasing the gap spacing, the value of the yield increases and reaches the highest values for the 1 μm gap size (blue triangles).

Figure 4a shows an increase of the effective yields with increasing the electric field illustrating that when the electric field near the cathode is sufficiently large, electrons

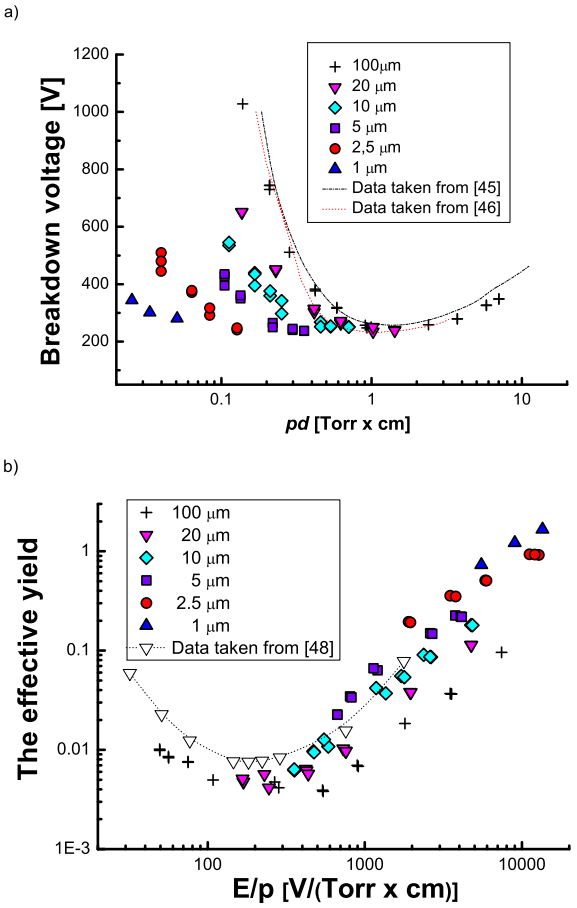

Fig. 3. (a) Breakdown voltage curves and (b) dependence of the electron yield on the inverted electric field for various gap sizes. Our results are compared with the experimental data taken from [45] and [46], respectively. Open down triangles correspond to the data taken from [48].

can be liberated from the surface by quantum mechanical tunneling. Due to the fact that the highest electric field is generated at the smallest gap spacing, the values of the yield are the highest for the 1 μm, while the lowest values are obtained for the 100 μm gap size. In order to illustrate the effect of the field emission on the secondary electron production we listed the minimum and maximum values of the effective yield for various gap sizes in Table 1. Following the data listed in Table 1, one may conclude that for the electrode gaps between 100 μm and 20 μm, the values of the effective yield are very similar to those for the centimeter distances [48]. For 10 μm gap size, the maximum value of the yield is around 0.2, while for the 2.5 μm is close to 1. On the other hand, for the gap 1 μm, the effective yields exceed the value 1 due to field emission effect.

The effective yields shown in Figure 4a can be fitted by the expression (1) in order to determine parameters K and D which could be than put into the expression (3) for calculating the breakdown voltages. Figure 4b demonstrates a good agreement between our experimental results

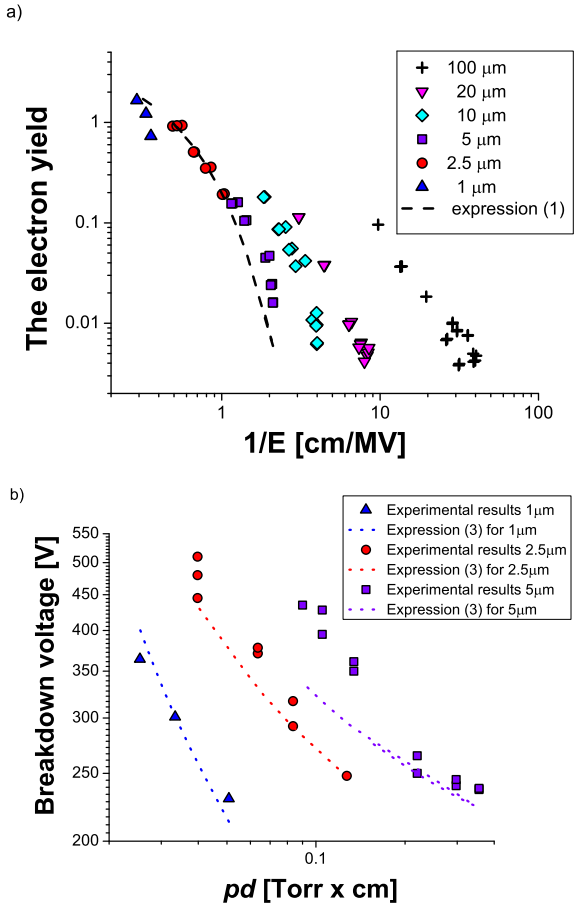

Fig. 4. (a) Dependence of the electron yield on the inverted electric field and (b) breakdown voltage curve determined in accordance with (2).

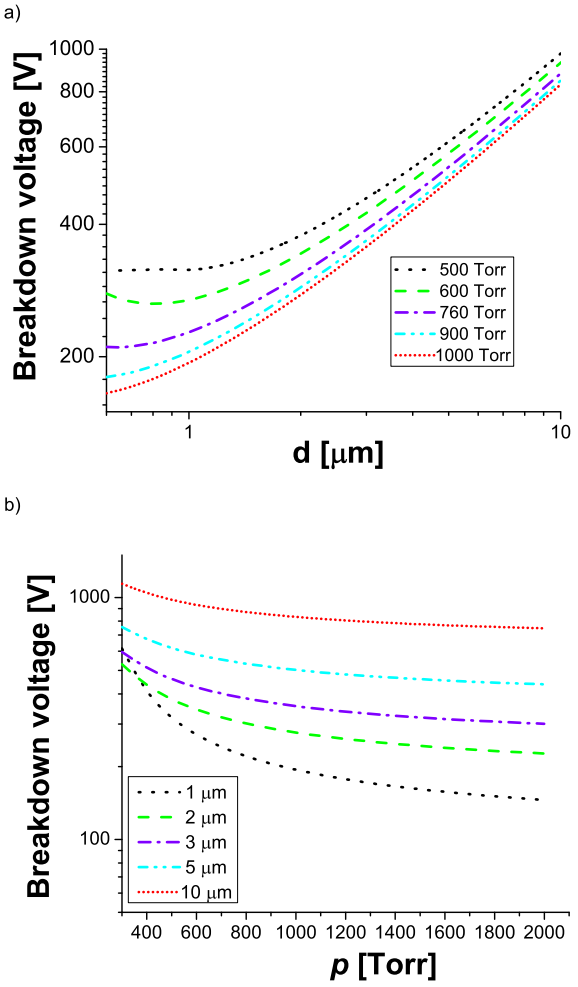

Fig. 5. Breakdown voltage calculated by using (3) as a function of: (a) the gap size (b) the pressure.

Table 1. The minimum and maximum values of the effective yield of argon estimated from the experimental data shown in Figure 3.

Gap size [μm]	γ_{min}	γ_{max}
100	0.0038	0.0958
20	0.0042	0.1137
10	0.0062	0.1802
5	0.0226	0.2254
2.5	0.1920	0.9348
1	0.7306	1.6578

(symbols) with the calculated values of the breakdown voltages (lines) under experimental conditions.

With determined parameters K and D and by using expression (3) it is easy to calculate the breakdown voltages under conditions where it is hard to establish proper experimental conditions as demonstrated in Figure 5 which contains calculated values of the breakdown voltage versus: (a) the gap spacing between 0.5 μm and 10 μm at various pressures and (b) the pressure in the range from 300 Torr to 2000 Torr for various gap sizes.

Figure 6 shows the ratio of the ion-enhanced field emission secondary coefficient γ' determined in accordance to expression (1) to Townsend's secondary coefficient γ (assumed average of 0.01) is plotted against: (a) the reduced electric field for various gap sizes and (b) the electrode gap for various values of K. The ratio of the yields γ'/γ extents many orders of magnitude as the breakdown transitions from Townsend dominated to field emission-dominated processes. As can be seen from Figure 6b, at larger gaps, when Paschen's curve holds true, the ratio is extremely small indicating that ion-enhanced field emission is negligible. However, for gaps ranged from approximately 3 μm until the peak voltage transition, the ratio is moderate indicating that though field emission is now important, Townsend secondary emission cannot be ignored. This suggests that breakdown begins deviating from Paschen's curve when emitted electrons are generated by ion-enhanced field emission rather than secondary emission. For gaps less then 3 μm the ratio becomes around 10^2 and for given γ that was fixed at 0.01, this corresponds to γ' larger then 1. A secondary emission coefficient larger then 1 is typically non-physical except in special cases, and this merely confirms that this description of breakdown is not appropriate at very small gaps.

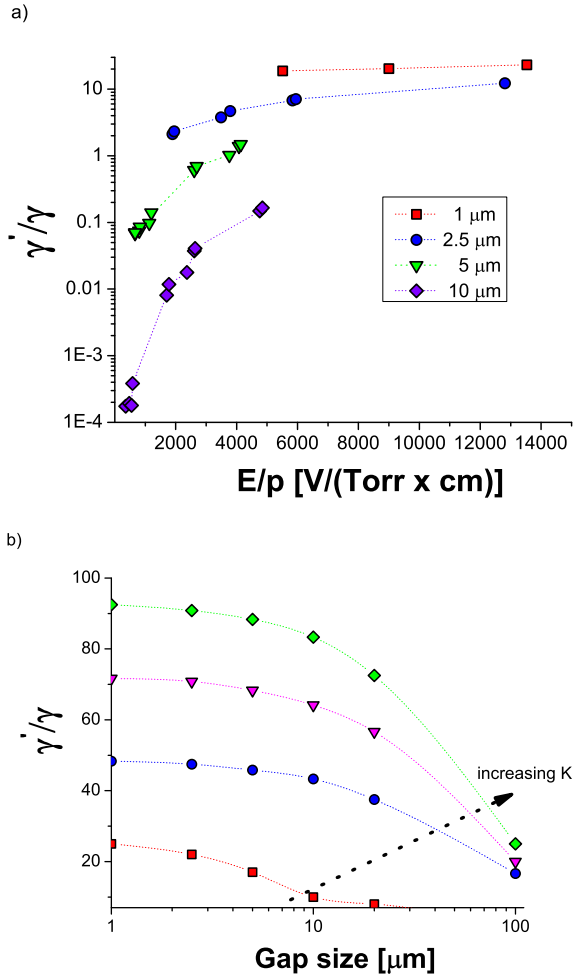

Fig. 6. Dependence of the γ'/γ on: (a) the reduced electric field at different gaps and (b) the gap size for different values of K. The $\gamma = 0.01$.

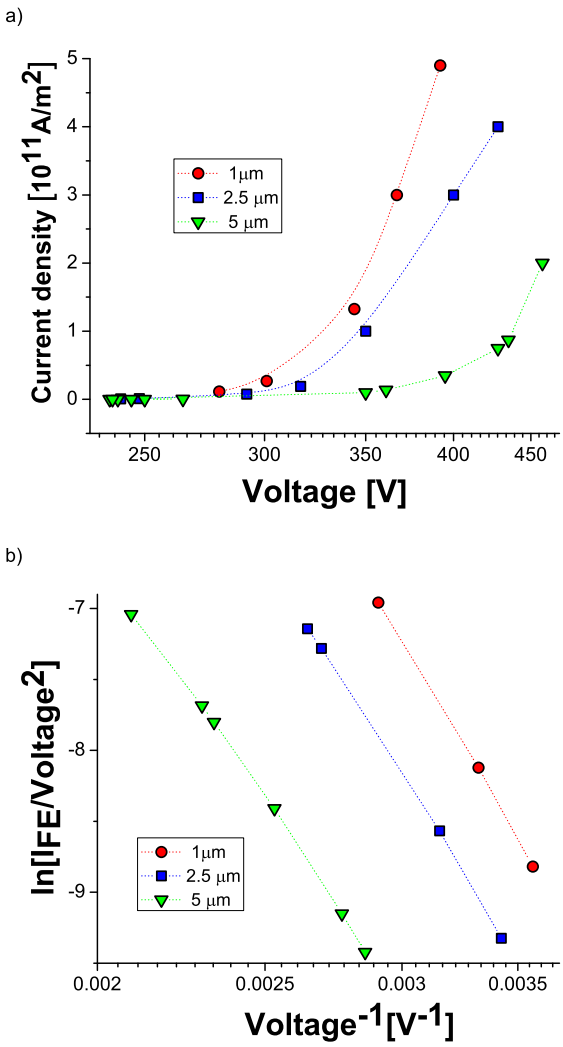

Fig. 7. (a) Current density and (b) F-N plot for various gap spacings determined from the expressions (4) and (9), respectively.

The F-N equation (4) correctly predicts the average current density at the gap sizes of the order of a few microns as demonstrated in Figure 7a. On the other hand, the negative slopes of the corresponding F-N plots (9) shown in Figure 6b confirm the that field emission plays significant role in such gap sizes. With increasing gap size, the breakdown voltage increases since the contribution of field emission progressively reduces.

Figure 8 contains current density for various work functions ϕ representing the effect of different electrode materials. The F-N current density decreases at the same applied voltage with increasing work function, while the space charge current density remains the same.

For a work function of 4.2 eV in case of molybdenum and a gap length of 2.5 μm, the F-N current density (blue symbols) obtained from the expression (4) and the space charge limited current density (red symbols) calculated from expression (11) are compared in Figure 9. The crossing point at around 1.4×10^8 V/m represents the transition field (transition from the F-N field emission to the space charge limited current density).

Due to the non-linear property of F-N equation (4), the geometric effects strongly affect the current density. The multiplication of β makes F-N current density (4) much larger, while the space charge limited current density remains unchanged. Consequently, the transition field is reduced. Figure 10 shows the approach to the space charge limited current density with increasing enhancement factor β. As the β factor increase, the current density also increases approaching the space charge limited current density.

Current-voltage characteristic and corresponding images of the development of discharge at the pressure of 205 Torr and the gap size of 20 μm are shown in Figure 11. From Figure 11a to Figure 11d, the V-A characteristic looks like typical current-voltage characteristic of low-pressure discharges with distinguished different discharge regions [49–51]. Image shown in Figure 11e corresponds to the arc discharge. Since the arc is expected at the pressure around one atmosphere, it seems to be some type

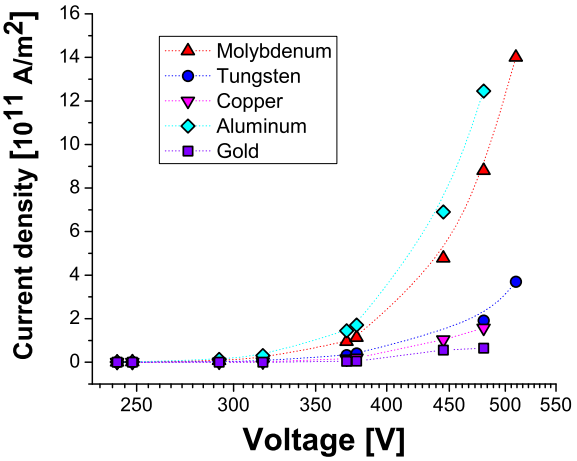

Fig. 8. F-N current density calculated in accordance with the expression (4) for the 2.5 μm gap size for the work function that corresponds to the various electrode materials.

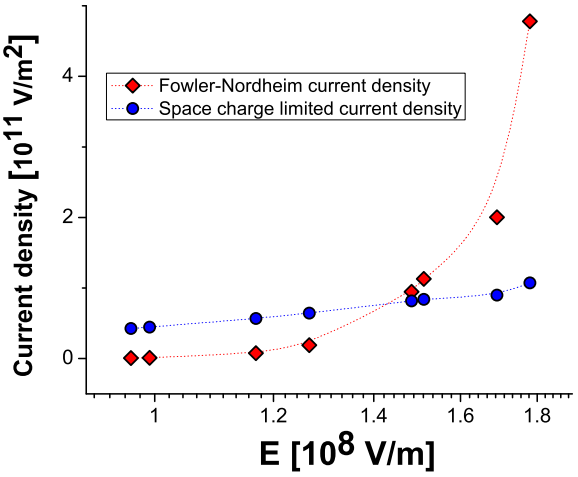

Fig. 9. F-N current density (red diamonds) and space charge limited current density (blue circles) plotted by using (4) and (11), respectively for the 2.5 μm gap size.

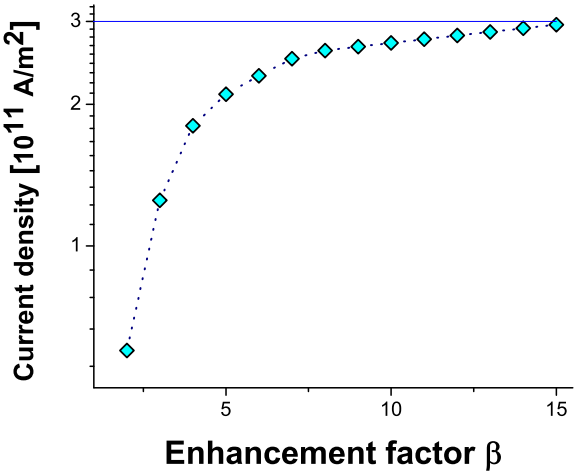

Fig. 10. Effect of the enhancement factor on approach to the space charge limited current density calculated for the 1 μm gap size and a fixed electric field of 2.5×10^9 V/m.

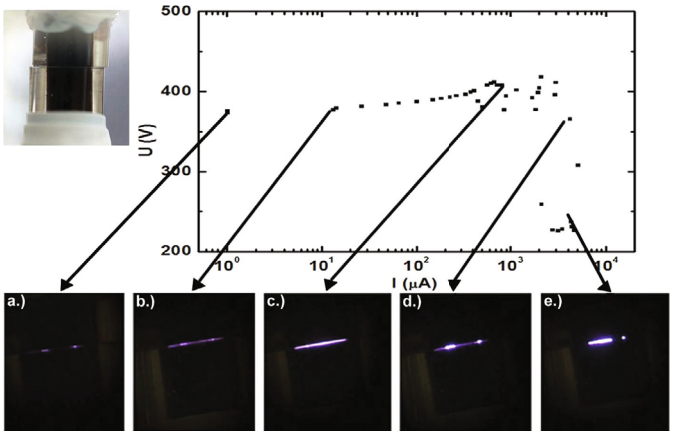

Fig. 11. Volt-Amper characteristics of the argon DC discharges at the gap size of 20 μm and the value of pd = 0.41 Torr cm.The exposure time was around 1 s.

of micro-arc, at somewhat lower pressures than usually. It could be explained as an explosion-like vaporisation of contact material being sometimes initiated by a micro-arc ignition [52–54]. As the discharge current increases, the electrodes start to melt and connect to each other.

5 Conclusions

In this paper we presented and discussed the measurements of the properties of DC argon microdischarges, including Paschen curves and Volt-Ampere characteristics. For the discharge gaps of the order of tens of microns, the breakdown voltage characteristics show a strong similarity to the results of low-pressure standard size discharges. For the lower gaps, however, breakdown is initiated by the secondary emission processes instead of a gas avalanche process. The observed breakdown voltage reduction may be attributed to the onset of ion-enhanced field emission. When the electric field becomes sufficiently large, the ion-enhanced field emission becomes dominant mechanism of the secondary emission process leading to the violation from the standard scaling law.

Values of the effective yields estimated from the measured breakdown voltage curves are spread from around 0.004 for the 100 μm up to around 1.7 for the 1 μm gap size indicating the importance of the ion induced field emission and field emission effect.

Theoretical predictions for the breakdown voltage curves, current densities and the space charge limited current density were also determined. Although the space charge limited current density does not depend on the work function, F-N current density strongly depends on the electrode material. With increasing the work function, F-N current density decreases and slowly approaches to the space charge limited current density.

The analysis of the Volt-Ampere characteristics and the corresponding images of the discharges recorded at

the gap size of 20 μm at $pd = 0.41$ Torr cm indicates the existence of micro-arcs at the pressure of around 200 Torr.

This work has been supported by the Vega 1/0514/12, the Slovak Research and Development Agency APVV -0733-11. M.R.-R. would like to acknowledge support by the National Scholarship Programme of the Slovak Republic funded by the Ministry of Education, Science, Research and Sport of the Slovak Republic. The work has also been carried out under Ministry of Education and Science 171037 project, Republic of Serbia. Numerical simulations were run on the PARADOX cluster at the Scientific Computing Laboratory of the Institute of Physics Belgrade.

References

1. U. Kogelschatz, Plasma Chem. Plasma Process. **23**, 1 (2003)
2. V. Karanassios, Spectrochim Acta Part B **59**, 909 (2004)
3. K.H. Becker, K.H. Schoenbach, J.G. Eden, J. Phys. D **39**, R55 (2006)
4. B. Mitra, B. Levey, Y.B. Gianchandani, IEEE Trans. Plasma Sci. **36**, 1913 (2008)
5. K. Hensel, Eur. J. Phys. D **54**, 141 (2009)
6. K.H. Becker, H. Kersten, J. Hopwood, J.L. Lopez, Eur. J. Phys. D **60**, 437 (2010)
7. C.K. Eun, G.Y. Gianchandani, IEEE J. Quantum Electron. **48**, 814 (2012)
8. K. Koseoglu, M. Ozer, B.G. Salamov, Plasma Process. Polymers **11**, 1018 (2014)
9. C.M. Du, M.D. Xiao, Sci. Rep. **4**, 7339 (2014)
10. A.M. Prochnow, A.B. Murphy, K.M. Mc Lean, M.G. Kong, K. Ostrikov, Int. J. Antimicrob. Agents **43**, 508 (2014)
11. M. Radmilović-Radjenović, B. Radjenović, IEEE Trans. Plasma Sci. **35**, 1223 (2007)
12. D. Mariotti, R.M. Sankaran, J. Phys. D. **43**, 323001 (2010)
13. M. Bashira, J.M. Rees, S. Bashir, W.B. Zimmerman, Phys. Lett. A **378**, 2395 (2014)
14. D.K. Olson, B.G. Peterson, G. Bryan, G.W. Hart, Rev. Sci. Instrum. **81**, 013507 (2010)
15. P. Bruggeman, R. Brandenburg, J. Phys. D **46**, 464001 (2013)
16. N. Škoro, J. Phys.: Conf. Ser. **399**, 012017 (2012)
17. D. Marić, N. Škoro, P.D. Maguire, C.M.O. Mahony, G.N. Malović, Z.Lj. Petrović, Plasma Sources Sci. Technol. **21**, 035016 (2012)
18. Z.Lj. Petrović, N. Škoro, D. Marić, C.M.O. Mahony, P.D. Maguire, M. Radmilović-Radenović, G. Malović, J. Phys. D **41**, 194002 (2008)
19. M. Radmilović-Radjenović, B. Radjenović, M. Klas, A. Bojarov, Š. Matejčik, Acta Phys. Slovaca **63**, 105 (2013)
20. M. Radmilović-Radjenović, Š. Metejčik, M. Klas, B. Radjenović, J. Phys. D **46**, 015302 (2013)
21. M. Klas, Š. Matejik, B. Radjenović, M. Radmilović-Radjenović, Phys. Scr. **83**, 045503 (2011)
22. Yu. Korolev, G.A. Mesyats, *Physics of Pulsed Breakdown in Gases* (URO-Press, Yekaterinburg, 1998)
23. V.A. Lisovskiy, S.D. Yakovin, V.D. Yegorenkov, J. Phys. D **33**, 2722 (2000)
24. A.V. Phelps, Z.Lj. Petrović, Plasma Sources Sci. Technol. **8**, R21 (1999)
25. M. Radmilović-Radjenović, J.K. Lee, F. Iza, G.Y. Park, J. Phys. D **38**, 950 (2005)
26. P. Rumbach, D.B. Go, J. Appl. Phys. **112**, 103302 (2012)
27. D.G. Marić, M.B. Savić, J. Sivoš, N. Škoro, M.D. Radmilović-Radjenović, G.N. Malović, Z.Lj. Petrović, Eur. J. Phys. D **68**, 155 (2014)
28. M. Klas, Š. Matejčik, B. Radjenović, M. Radmilović-Radjenović, Phys. Plasmas **21**, 103503 (2014)
29. R.E. Burgess, H. Kroemer, Phys. Rev. **90**, 515 (1953)
30. K. Yuasa, A. Shimoi, I. Ohba, C. Oshima, Surf. Sci. **520**, 18 (2002)
31. A.J. le Febre, L. Abelmann, J.C. Lodder, J. Vac. Sci. Technol. B **26**, 724 (2008)
32. M. Klas, Š. Matejčik, B. Radjenović, M. Radmilović-Radjenović, Phys. Lett. A **376**, 1048 (2012)
33. Y. Li, D.B. Go, J. Appl. Phys. **116**, 103306 (2014)
34. W.S. Boyle, P. Kisliuk, Phys. Rev. **97**, 255 (1955)
35. M. Radmilović-Radjenović, B. Radjenović, Plasma Sources Sci. Technol. **17**, 024005 (2008)
36. M. Radmilović-Radjenović, B. Radjenović, Europhys. Lett. **83**, 25001 (2008)
37. V.A. Lisovskiy, V.D. Yegorenkov, J. Phys. D **27**, 2340 (1994)
38. M. Radmilović-Radjenović, B. Radjenović, Š. Matejčik, M. Klas, Plasma Chem. Plasma Process. **34**, 55 (2014)
39. A. Khademi, R. Azimirad, Y.-T. Nien, A.Z. Moshfegh, J. Nanopart. Res. **13**, 115 (2011)
40. M. Radmilović-Radjenović, B. Radjenović, Š. Matejčik, M. Klas, Europhys. Lett. **103**, 45002 (2013)
41. D.B. Go, A. Venkattraman, J. Phys. D **47**, 503001 (2014)
42. R.G. Forbes, A. Fischer, M.S. Mousa, J. Vac. Sci. Technol. B **31**, 02B103 (2013)
43. Y. Feng, J.P. Verboncoeur, Phys. Plasmas **13**, 073105 (2006)
44. M. Radmilović-Radjenović, B. Radjenović, M. Klas, Š. Matejčcik, Micro Nano Lett. **7**, 232 (2012)
45. J.M. Meek, J.D. Craggs, *Electrical breakdown of gases* (Oxford University Press, Oxford, 1953)
46. V.A. Lisovsky, S.D. Yakovin, J. Exp. Theor. Phys. Lett. **72**, (2000) 34
47. Ph. Guillot, Ph. Belenguer, L. Therese, V. Lavione, H. Chollet, Surf. Interface Anal. **35**, 604 (2003)
48. G. Auday, Ph. Guillot, J. Galy, H. Brunet, J. Appl. Phys. **83**, 5917 (1998)
49. C. Bruno, Y. Jian-Hua, M. Zeng-Yi, P. Xin-Chao, C. Ke-Fa, T. Xin, Acta Phys. Sin. **55**, 3451 (2006)
50. Y. Yin, M.M.M. Bilek, D.R. McKenzie, R.W. Boswell, C. Charles, J. Phys. D **37**, 2871 (2004)
51. X. Li, R. Liu, P. Jia, W. Bao, Y. Shang, Europhys. Lett. **102**, 55003 (2013)
52. A.S. Kumar, K. Okazaki, IEEE Trans. Plasma Sci. **23**, 735 (1995)
53. Y. Hirata, M. Fukushima, T. Sano, K. Ozaki, T. Ohji, Vacuum **59**, 142 (2000)
54. M. Park, Y. Hirata, T. Urabe, Weld. World **58**, 47 (2014)